Received: 1 February 2022 | Revised: 12 May 2022 | Accepted: 25 May 2022

DOI: 10.1002/mp.15792

RESEARCH ARTICLE

MEDICAL PHYSICS

Performance evaluation of side-by-side optically coupled monolithic LYSO crystals

Marta Freire | **Sara Echegoyen** | **Andrea Gonzalez-Montoro** | **Filomeno Sanchez** | **Antonio J. Gonzalez**

Instituto de Instrumentación para Imagen Molecular (I3M), Centro Mixto CSIC - Universitat Politècnica de València, Valencia, Spain

Correspondence
Marta Freire, Instituto de Instrumentación para Imagen Molecular (I3M), Camino de Vera s/n, Ed. 8B, Acc. N, Niv. 0, 46022 Valencia, Spain.
Email: mfreire@i3m.upv.es

Funding information
Ministerio de Ciencia, Innovación y Universidades (MCIU), Grant/Award Number: PID2019-107790RB-C21; Foundation for the National Institutes of Health (FNIH), Grant/Award Number: 1R01EB029450-01; EC | Emprego, Assuntos Sociais e Inclusão | European Social Fund (ESF), Grant/Award Number: IDIFEDER/2021/004

Abstract

Background: Significant interest has been recently shown for using monolithic scintillation crystals in molecular imaging systems, such as positron emission tomography (PET) scanners. Monolithic-based PET scanners result in a lower cost and higher sensitivity, in contrast to systems based on the more conventional pixellated configuration. The monolithic design allows one to retrieve depth-of-interaction information of the impinging 511 keV photons without the need for additional hardware materials or complex positioning algorithms. However, the so-called edge-effect inherent to monolithic-based approaches worsens the detector performance toward the crystal borders due to the truncation of the light distribution, thus decreasing positioning accuracy.

Purpose: The main goal of this work is to experimentally demonstrate the detector performance improvement when machine-learning artificial neural-network (NN) techniques are applied for positioning estimation in multiple monolithic scintillators optically coupled side-by-side.

Methods: In this work, we show the performance evaluation of two LYSO crystals of $33 \times 25.4 \times 10$ mm^3 optically coupled by means of a high refractive index adhesive compound (Meltmount, refractive index $n = 1.70$). A 12×12 silicon photomultiplier array has been used as photosensor. For comparison, the same detector configuration was tested for two additional coupling cases: (1) optical grease ($n = 1.46$) in between crystals, and (2) isolated crystals using black paint with an air gap at the interface (named standard configuration). Regarding 2D photon positioning (XY plane), we have tested two different methods: (1) a machine-learning artificial NN algorithm and (2) a squared-charge (SC) centroid technique.

Results: At the interface region of the detector, the SC method achieved spatial resolutions of 1.7 ± 0.3, 2.4 ± 0.3, and 2.6 ± 0.4 mm full-width at half-maximum (FWHM) for the Meltmount, grease, and standard configurations, respectively. These values improve to 1.0 ± 0.2, 1.2 ± 0.2, and 1.2 ± 0.3 mm FWHM when the NN algorithm was employed. Regarding energy performance, resolutions of $18 \pm 2\%$, $20 \pm 2\%$, and $23 \pm 3\%$ were obtained at the interface region of the detector for Meltmount, grease, and standard configurations, respectively.

Conclusions: The results suggest that optically coupling together scintillators with a high refractive index adhesive, in combination with an NN algorithm, reduces edge-effects and makes it possible to build scanners with almost no gaps in between detectors.

KEYWORDS
monolithic scintillator, neural network, optical coupling, PET, position estimation

1 | INTRODUCTION

The two most prevalent geometry configurations of scintillation crystals used on conventional gamma-ray scanners are the pixelated and the monolithic.[1] Pixelated crystal configurations are the most extended configuration in positron emission tomography (PET) scanners, since it allows for a relatively easy pixel identification. Nevertheless, monolithic scintillators offer lower cost, higher sensitivity, and provide intrinsic depth-of-interaction (DOI) information of the gamma-ray interaction within the scintillator, thus enabling the possibility to correct for parallax errors.[2] Moreover, monolithic-based designs allow one to accurately characterize the scintillation light distributions (LDs) and, thus spatial resolutions of 1 mm have already been obtained.[3] As a consequence of all these features, a significant interest has grown over the recent years for using gamma-ray scanners based on monolithic crystals for both academic and commercial purposes.[4–11]

In both the pixelated and monolithic approaches, the gaps in between detectors decrease system sensitivity. Moreover, the performance of monolithic scintillators tends to be compromised toward the crystal edges (border effect)[12] due to the strongest truncation of the LD in these areas. Therefore, data recorded at the edges have a poorer performance and are eventually discarded,[13–15] thus, reducing the useful detector volume and consequently decreasing the system sensitivity.

Several methods have been developed to mitigate border effects, some of them are based on weighted centroid methods[16] or squared-charge (SC) centroids.[17] Recently, the development of multichannel photosensor-readout application-specific integrated circuits combined with silicon photomultipliers (SiPMs) enabled the possibility to build highly granular, scalable, and large arrays for position sensitive gamma-ray detectors.[18–20] These developments allowed for an exhaustive characterization of the 3D spatial detector response, paving the way for new positioning algorithms, such as maximum-likelihood (ML) methods,[21,22] nonlinear data fit,[23] k-NN technique,[24,25] Voronoi-based calibration methods,[26] and machine-learning artificial neural-network (NN) algorithms.[27–29] However, these new algorithms only partially alleviate edge-artifacts and, thus, these effects are still present,[30] particularly when using thick scintillators. The use of bigger monolithic crystals would be a good approach; however, this presents some limitations in crystal growth size and geometrical flexibility in ring construction. A proposed solution is to optically couple side-by-side monolithic crystals.[31,32] A previous simulation study demonstrated that using optical coupling compounds with refractive index approaching the refractive index of the scintillation crystal allows the scintillation light to spread through the crystal junctions almost preserving the shape of the LD and, therefore, reducing substantially edge-artifact.[31] In addition to this, optically coupling monolithic crystals reduces the gaps in between detectors, thus increasing sensitivity; and overcomes the challenges in using large scintillator volumes. Other authors have experimentally evaluated the use of optical adhesive to couple LYSO monolithic blocks, and generated look up tables followed by a least-squares minimization and ML methods for event positioning.[32] They have also concluded that the adoption of optically coupled monolithic crystals can be a useful and feasible method to improve the uniformity of performances in the whole sensitive area.[32]

In this work, we have experimentally evaluated, as a proof-of-concept, the performance of a detector based on a 12 × 12 SiPM array and two LYSO crystals of 33 × 25.4 × 10 mm^3 optically coupled by means of a high refractive index compound (refractive index $n = 1.70$). This configuration was compared to two additional coupling methods, namely: (1) optical grease (refractive index $n = 1.46$) between crystals and (2) isolated blocks using black paint and air interface. For XY event positioning, we have tested two different methods: (1) SC centroid technique, which is a modified Anger logic procedure that has demonstrated enhanced linearity and spatial resolution,[16] and (2) machine-learning artificial NN algorithm. The performance of the optically coupled system was evaluated in terms of spatial linearity and resolution (including DOI determination) as well as energy performance.

2 | MATERIALS AND METHODS

For the experimental setup, two $(LuY)_2SiO_5$ (LYSO) crystals of 33 × 25.4 × 10 mm^3 with refractive index of 1.81 from EPIC Crystals Co., Ltd, China, were used. All crystal faces were polished and black painted except one of 33 × 10 mm^2 that was rough. The two crystals were coupled along this face.

Three configurations were tested; in the first one, a high refractive index compound named "Cargille Meltmount" ($n_{Meltmount} = 1.70$) was used.[33] Meltmount is a thermal plastic material, thus its viscosity is inversely dependent on the temperature. Therefore, it was heated to 70°C on a hotplate to decrease its viscosity. The two sides of the crystals to be glued were also heated to avoid sudden temperature changes when applying the

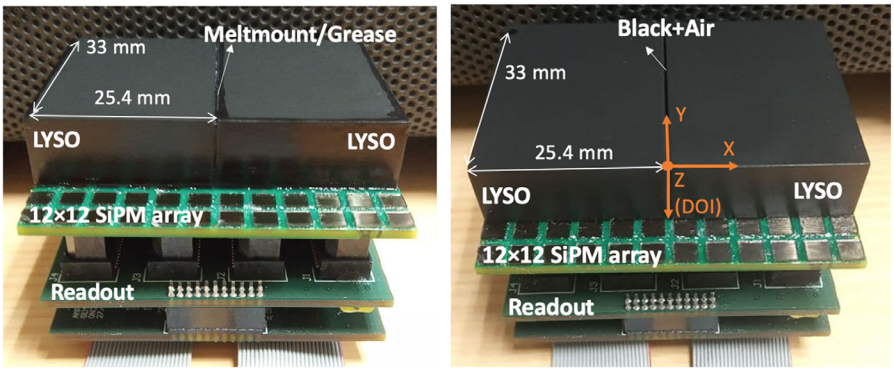

FIGURE 1 Detector configurations used in this work. (a) Meltmount or grease configuration, where all lateral faces were painted black except the interface one that was used to coupled crystals. (b) Standard configuration, where all the lateral faces of the crystal were painted black

TABLE 1 Refractive index and optical properties of the materials used in this work

Material	Optical properties at the interface	Refrective index
LYSO	–	$n_{LYSO} = 1.81$
Black paint	Absorption	–
Grease	Partial transmission	$n_{grease} = 1.46$
Meltmount	Partial transmission	$n_{Meltmount} = 1.70$
Air	Partial transmission	$n_{air} = 1.00$

Meltmount compound. When the targeted temperature was reached, the Meltmount compound was spread in the side of one of the crystals using a spatula and was immediately attached to the side of the other crystal. Then, the coupled crystals cooled down to room temperature. For the second configuration, named optical grease, the crystals were coupled together using "SS-988 Non-Curing Optical Coupling Gel - V-788 Offset" ($n_{grease} = 1.46$) from Silicone Solutions.[34] For the third configuration, named standard configuration, these side faces of the crystal were black painted and placed together letting an air gap between them. For all cases, the gap between the two faces was 0.5 mm (Figure 1). Table 1 summarizes the refractive index and optical properties of the different used compounds.

In all cases, the exit face of the crystals was coupled by means of optical grease to a 12 × 12 SiPMs array (SensL, now OnSemi) with 3 × 3 mm^2 active area each and a pitch of 4.2 mm. Each SiPM array was directly connected to a readout circuit that provides output signals for each column (c_i) and row (r_i) of the photosensor array.[6] Notice that only the eight central rows were covered by scintillation crystals and, thus, only those were read out (Figure 1). These signals are digitized using custom analog-to-digital converter (ADC) boards (12-bit precision and 250 ns integration time) providing information for both *x* and *y* projections of the LD.

The detector performance was studied through coincidence measurements using a reference detector based on a LYSO crystal of 50 × 50 × 15 mm^3. The reference detector was coupled to an identical 12 × 12 SiPMs array. Coincidence data were acquired using a ^{22}Na pencil beam (450 μm slit) generated using a ^{22}Na source of 1 mm in diameter with an activity of about 7 μCi, attached to a mechanical collimator composed of two tungsten blocks of 56 × 56 × 30 mm^3 separated by the slit (Figure 2). The slit collimator was moved in steps of 0.5 mm along the *x* and *y* directions. For the scan along the *y* direction, the studied detector was rotated 90°. The acquisition time was 1000 s for each slit position. We have scanned the slit along each direction started and ended outside the crystal to ensure that the entire scintillation volume was scanned. Plotting the number of events as a function of the slit position, the borders of the crystals can be found, and the real position of the slit determined. A total of 101 slit positions in *x* direction and 64 positions in *y* direction covered the detector under study (Figure 2).

2.1 | XY positioning, DOI, and energy estimation

For the 2D positioning of the scintillation events in the crystals, the *x* and *y* coordinates were calculated using

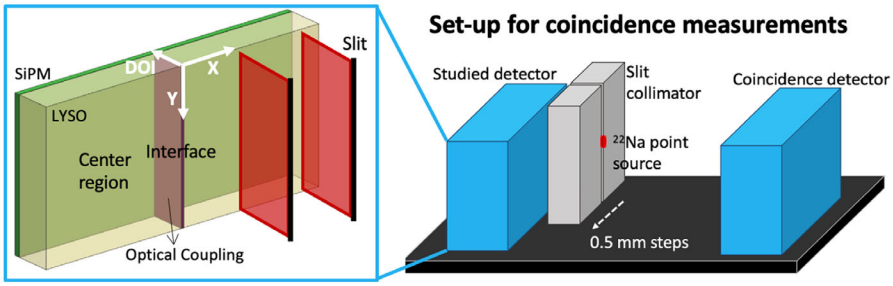

FIGURE 2 Sketch of the experimental setup showing the ^{22}Na point source in front of the slit collimator (thickness of 30 mm), the studied detector composed by two LYSO crystals coupled to an array of 12 × 12 SiPMs and the reference detector for coincidence measurements. The fan beam was scanned on 0.5 mm steps in both the *x* and *y* directions

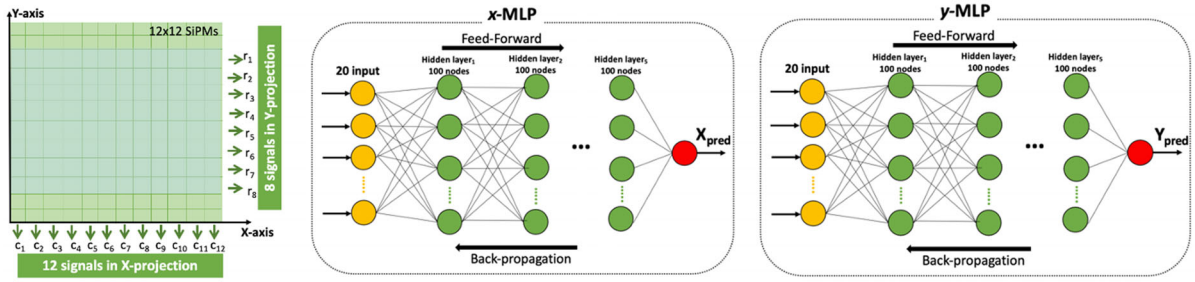

FIGURE 3 Each MLP was trained using the slit measurement along *x* and *y* direction, respectively. The MLPs contain 20 inputs, corresponding to the signals along *x* and *y* projections, five layers, 100 nodes each, and one output corresponding to the predicted coordinate

both the SC and the NN positioning methods. For the NN method, one multilayer perceptron architecture (MLP) was used for each direction, named *x*-MLP and *y*-MLP, respectively (Figure 3). Both MLPs contain five hidden layers and 100 nodes. The inputs of the networks are the digitized SiPM projection signals, thus 12 signals for *x* projection and 8 signals for *y* projection were included. The slit measurement along the *x* and *y* directions was used to train the *x*-MLP and *y*-MLP, respectively. Two filters were applied to the data:

- Energy filter: The energy was calculated for each individual event as the mean of the sum of signals for *x* and *y* projections. For each slit position, only the events that fell within ±15% of the energy spectra photopeak were considered.
- Position filter: The coordinates were pre-estimated using the center-of-gravity (CoG) algorithm.[35] The CoG_x and CoG_y ensemble distribution of each slit position was obtained for the scanning along *x* and *y* directions, respectively. Events outside the 10% of the peak ensemble distribution along each direction were removed in order to discard events that have suffered Compton scatter, or other interactions, before photoelectric absorption.[36]

After these prefilters, the dataset, that contains about 7k events per slit position, was split into three datasets: *train* (50%), *evaluation* (5%), and *test* (45%). Each MLP was trained using the *train* dataset by the Adagrad optimizer using rectified linear activation function (RELU) and the root mean squared median (RMSE) loss function:

$$RMSE = \sqrt{\frac{\sum_{i=1}^{N} \left(pos_{real}(i) - pos_{pred}(i)\right)^2}{N}}, \quad (1)$$

where N is the number of events, pos_{real} is the real position of the slit in mm, and pos_{pred} is the predicted position also in mm. After training, the MLP was evaluated using the *evaluation* dataset to avoid overfitting.

In the SC algorithm, the x_c and y_c coordinates from the *test* dataset were first estimated using the following equations:[17]

$$x_c = \frac{\sum_{i=1}^{i=12} c_i^2 x_i}{\sum_{i=1}^{i=12} c_i^2}, \quad (2)$$

$$y_c = \frac{\sum_{i=1}^{i=8} r_i^2 y_i}{\sum_{i=1}^{i=8} r_i^2}, \quad (3)$$

where c_i and r_i are the digitized signals for the projected columns and rows, respectively, and x_i and y_i are the SiPM positions on the detection surface. Acquired data moving the slit along the *x* and *y* directions were used

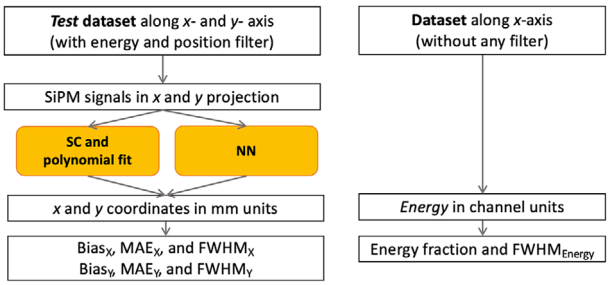

FIGURE 4 Diagram of the dataset employed and calculated parameters for the detector evaluation in terms of spatial and energy performance

to calibrate the estimated x_c and y_c coordinates into mm units. The position profile was fitted using a Gaussian distribution, and the centroid of each measurement was recorded. The slit real position was plotted versus the estimated centroids and a third polynomial fit was used to convert the measured units to mm (see sketch in Figure 4).

The gamma-ray energy (E) was calculated as the mean of the sum of signals for x and y projections. The gamma-ray impact DOI was estimated by using its correlation with the width of the LD profiles and a model of the light transport in the crystal. It is calculated as the average of the ratio of the energy to the maximum signal value (E/I_{max}) for x and y projections.[37]

2.2 | Spatial and energy performance

For each tested configuration, the x and y coordinates from the *test* dataset along the x- and y-axis (containing the LD profiles after energy and position filter) were calculated using the two studied positioning methods (see sketch in Figure 4). The following parameters along each direction were calculated for each slit measurement:

- Bias$_X$ and Bias$_Y$, calculated as the difference between the estimated position, $x_{estimated}$ *or* $y_{estimated}$, and the known position, x_{real} *or* y_{real}:

$$Bias_X = \frac{1}{N} \times \sum_{i=1}^{i=N} \left(x_{estimated}(i) - x_{real}(i)\right) \quad (4)$$

$$Bias_Y = \frac{1}{N} \times \sum_{i=1}^{i=N} \left(y_{estimated}(i) - y_{real}(i)\right) \quad (5)$$

- Mean average error, MAE$_X$ and MAE$_Y$, was calculated following the equations:

$$MAE_X = \frac{1}{N} \times \sum_{i=1}^{i=N} \left|x_{estimated}(i) - x_{real}(i)\right|, \quad (6)$$

$$MAE_Y = \frac{1}{N} \times \sum_{i=1}^{i=N} \left|y_{estimated}(i) - y_{real}(i)\right|, \quad (7)$$

where N is the number of events for each slit measurement.

- Spatial resolution, FWHM$_X$ and FHWM$_Y$, calculated as the FWHM of the Gaussian fit to the $x_{estimated}$ and $y_{estimated}$ distribution, respectively.

Regarding the DOI performance, we have plotted the E/I_{max} histograms for each slit measurement of the dataset along x-axis (with only energy filter applied) and fitted them using the following analytical expression:[38]

$$DOI\ (z) = A \times e^{-\alpha z}\left[\mathrm{erf}\left(\frac{b-z}{\sqrt{2}\sigma_{int}}\right) - \mathrm{erf}\left(\frac{a-z}{\sqrt{2}\sigma_{int}}\right)\right], \quad (8)$$

where α is the attenuation coefficient of the material, A is the amplitude, σint is the standard deviation of the distribution which relates to the DOI FWHM as 2.35×σint, erf is the Gaussian error function, and a and b are the lower and upper limits of the distribution.

Regarding energy performance, a Gaussian fit to the energy spectra (without any filter) was applied to the data at each slit position of the dataset along x-axis to obtain the photopeak position ($E_{photopeak}$) in energy channels. The photopeak position value corresponding to the slit at the center crystal ($E_{photopeak,center}$) was used to calculate the energy fraction parameter for each slit position, as $E_{photopeak}/E_{photopeak,center}$. Notice that this parameter was calculated for each side of the interface separately. The energy resolution was obtained as $\Delta E(FWHM)/E_{photopeak}$.

For each configuration, the average and standard deviation of the parameters described in this section were also calculated.

3 | RESULTS

3.1 | Light distribution

The shape of the measured LD varies depending on the detector configuration.[31] For the standard configuration (see experimental examples for one gamma-ray impact at 0.5 mm to the left of the interface in Figure 5a), most of the generated scintillation light is absorbed by the black paint and, therefore, the LD is truncated. When the crystals were coupled using the high refractive index compound, the light can travel to the neighbor crystal and be collected by the SiPMs located at the right of the interface (Figure 5b). However, there is not glue compound, to our knowledge, perfectly matching the refractive index of the LYSO scintillator and, therefore, some scintillation light is still reflected at the interface by

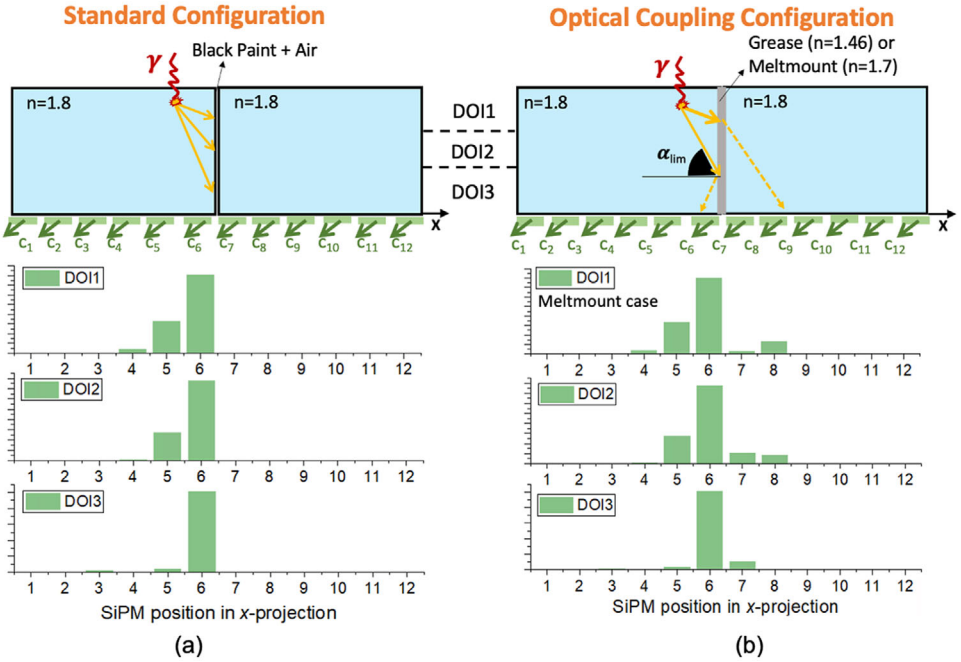

FIGURE 5 Example of LD profiles for impacts near the interface (0.5 mm) for different DOI positions. (a) LD profiles for the standard configuration. (b) LD profiles for the Meltmount configuration

this index unmatching. The amount of light transmitted to the neighbor crystal depends on the difference of such refractive indexes between the crystal and the coupling compound. The outcome of this reduced transmission is a discontinuity in the LDs (Figure 5b) that needs to be modeled in the detector calibration.

3.2 | Spatial and energy performance

The bias_X, MAE_X, and FWHM_X values along the *x*-axis are shown in Figure 6 for both the SC and NN positioning estimation methods. The values corresponding to slit positions belonging to the range between –3 and 3 mm, named the interface region, are shown in Figure 7. It can be observed that bias_X, MAE_X, and FWHM_X are significantly improved near the optical coupling interface when using Meltmount compound.

Figure 8 shows the average values of the $|\text{bias}_X|$, MAE_X, and FWHM_X for the slit positions at the interface region (3 mm from the optical coupling to each side) as well as their standard deviation (error bars) for each configuration. Using the SC method, a spatial resolution of 1.7 ± 0.3, 2.4 ± 0.3, and 2.6 ± 0.4 mm FWHM was obtained for the Meltmount, grease, and standard configurations, respectively. Lower values are found when the impact positions are estimated using the NN and when the crystals are optically coupled using Meltmount, achieving a FWHM_X of 1.0 ± 0.2 mm.

The bias_Y, MAE_Y, and FWHM_Y values for the slit position along the *y*-axis are plotted in Figure 9. The mean values of the parameters for all slit positions along *y*-axis and their standard deviations are shown in Figure 10. Best values were found for NN method for all the configurations, as it occurs along *x*-axis.

The left panel in Figure 11 shows the DOI histograms (in arbitrary DOI units) measured for one slit position at the crystal center (15 mm from the optical coupling) and other at the interface (1 mm from the optical coupling) for the Meltmount, grease, and standard configurations. The profiles were fitted using Equation (8), see green lines.

Figure 12a shows the energy spectra (normalized to the maximum value) corresponding to one slit position at the center region as well as at the interface region for the three studied configurations, in ADC units. The energy fraction and resolution are also shown in Figure 12b. For all configurations near the coupling interface, more energy losses are observed compared to the center of each crystal (energy fraction values close to 1). However, for the Meltmount configuration, these losses are lower compared to the other configurations. Moreover, better energy resolution values were obtained at the interface region for the Meltmount configuration. Figure 12c shows the average and standard deviation values for slit positions at the interface region. The standard configuration exhibited lower (20% on average) photopeak values. These differences are reduced when using grease as optical coupling and are almost vanished using Meltmount. Average energy resolutions at the interface region of 18 ± 2%, 20 ± 2%, and 23 ± 3% were measured for the Meltmount, grease, and standard configurations, respectively.

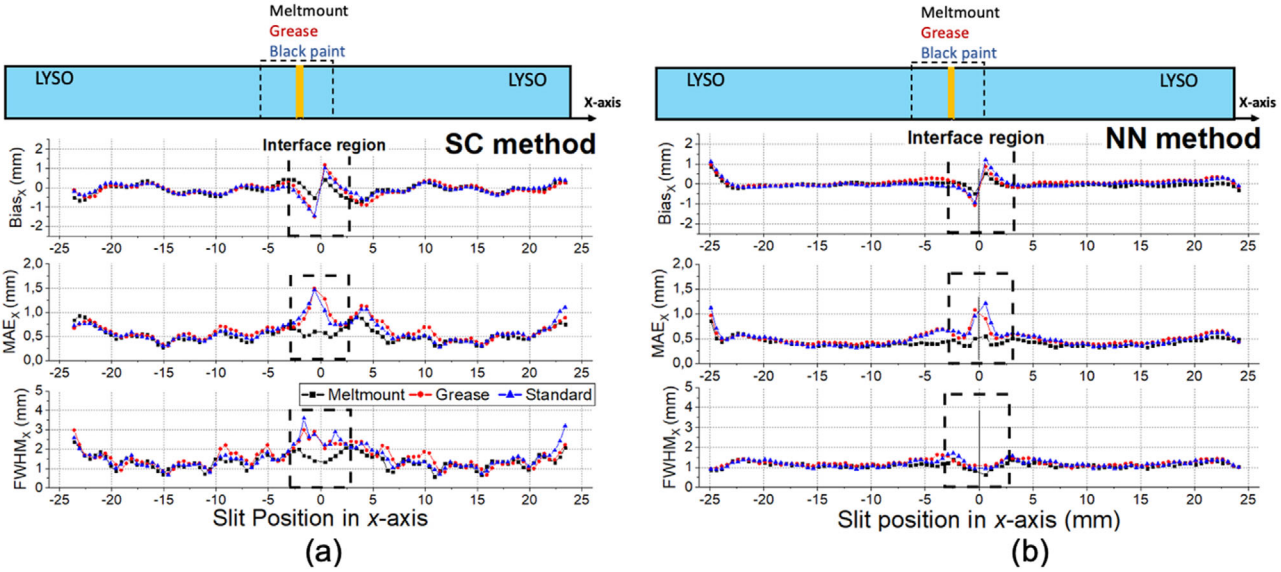

FIGURE 6 Bias$_X$, MAE$_X$, and FWHM$_X$ as a function of the slit position along the *x*-axis for the three configurations, using SC (a) and NN (b) position estimation methods

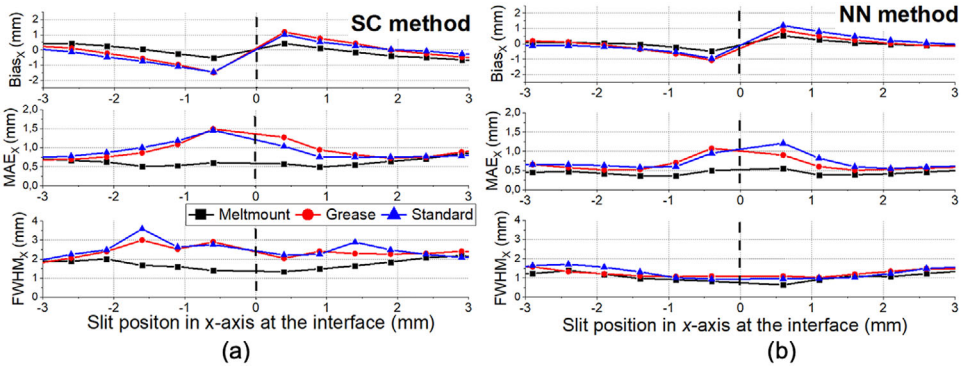

FIGURE 7 Bias$_X$, MAE$_X$, and FWHM$_X$ as a function of the slit position at the interface region along the *x*-axis for the three configurations, using SC (a) and NN (b) position estimation methods

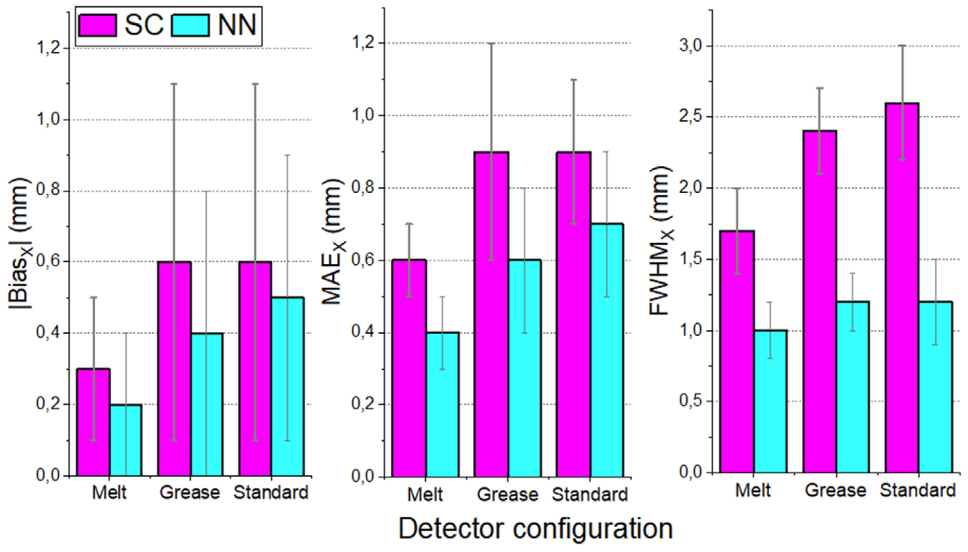

FIGURE 8 Average and standard deviation (error bars) values of the |bias$_X$|, MAE$_x$, and FWHM$_x$ corresponding to the slit positions at the interface region for each position estimation method

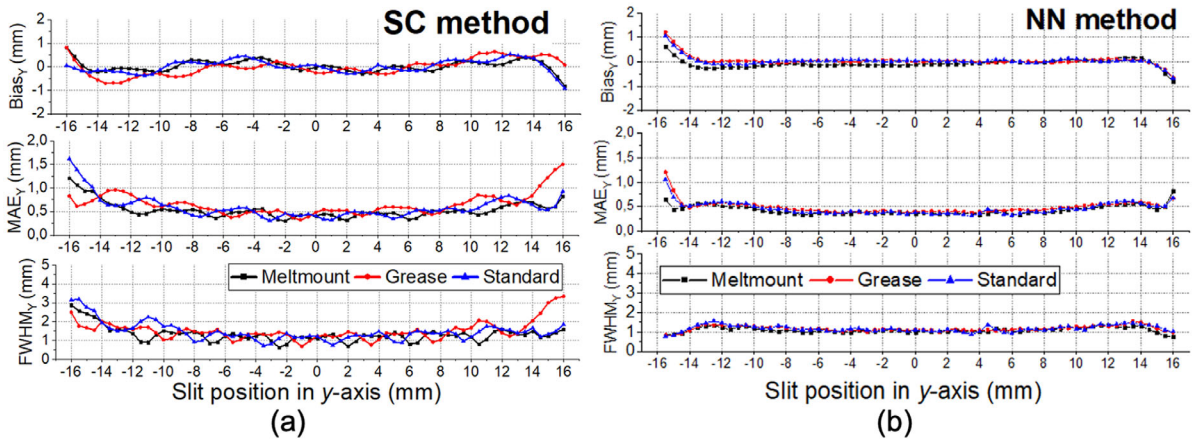

FIGURE 9 Bias$_Y$, MAE$_Y$, and FWHM$_Y$ as a function of the slit position along the *y*-axis for the three configurations, using SC (a) and NN (b) position estimation methods

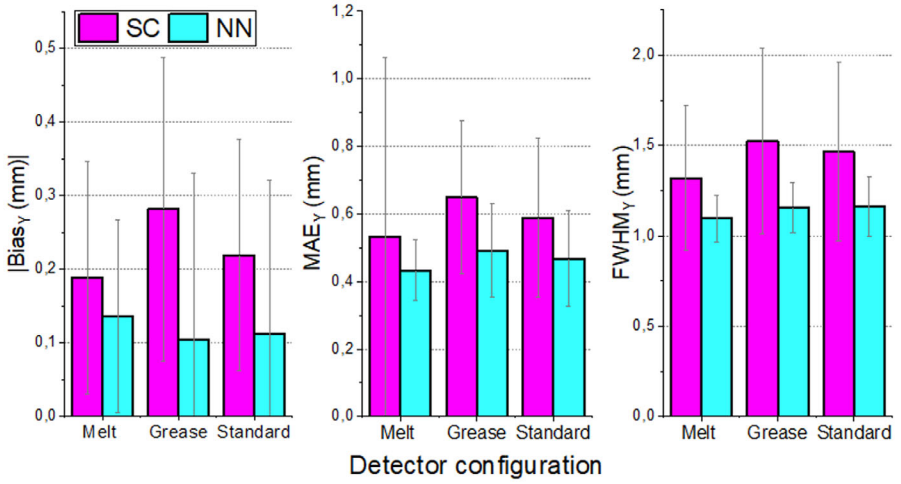

FIGURE 10 Average and standard deviation (error bars) values of the |bias$_Y$|, MAE$_Y$, and FWHM$_Y$ corresponding to all the slit positions in *y*-axis for each position estimation method

FIGURE 11 DOI histograms (in arbitrary DOI units) measured for one slit position at the crystal center (15 mm from the optical coupling) and other at the interface (1 mm from the optical coupling) for the Meltmount, grease, and standard configurations. The profiles were fitted using Equation (8), see green lines

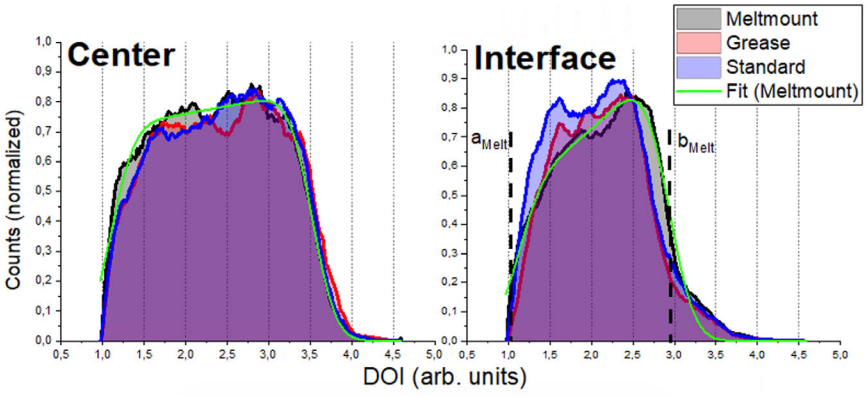

4 | DISCUSSION

In this work, we have experimentally evaluated the performance achieved when coupling two monolithic LYSO crystals using Meltmount ($n_{Meltmount}$ = 1.7), optical grease (n_{grease} = 1.46), and air (standard configuration) between them, in terms of spatial (including DOI) and energy performance. In all cases, the crystals were

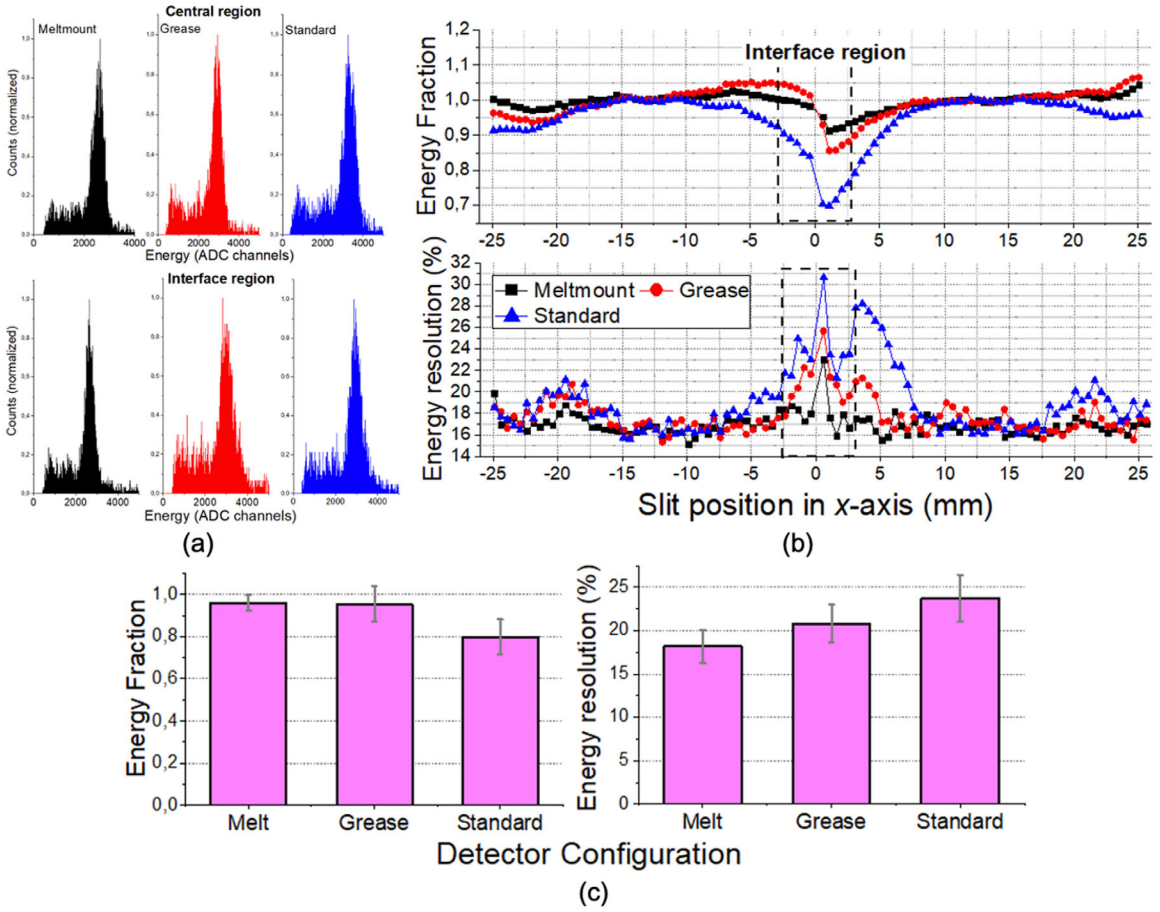

FIGURE 12 (a) Energy spectra for one slit at the center of one crystal and at the interface region. (b) Energy fraction and resolution as a function of the slit position along the *x*-axis. (c) Average and standard deviation (error bars) values of energy fraction and resolution for slit positions at the interface region

coupled to a 12 × 12 SiPMs array and read out with a circuit that provides each row and column signals of the photosensor.

For the planar coordinates (XY), two positioning estimation methods were compared, named SC and NN. Figure 8 shows that the $|\text{bias}_X|$, MAE_X, and FWHM_X improved near the interface for the case with smaller mismatch with the refractive index of the crystal, that is, Meltmount configuration. In this case, the total internal reflection is minimal, allowing a better LD characterization and thus, reducing the edge-effect, as expected. Moreover, the NN technique improves the spatial performance along *x*- and *y*-axis compared to the SC method (Figures 8 and 10). The NNs are able to learn the LD shapes from all the samples of the training data, and thus, a higher spatial accuracy is expected in contrast to SC method, despite having applied a third polynomial fit to mitigate border effects. However, quite similar performance in terms of bias_X, MAE_X, and FWHM_X has been obtained for the grease and standard configuration at the interface region (Figure 6). We hypothesize that such a similar behavior is explained by the filter of 10% in positions that may be masking the differences of these two configurations. Higher LD truncation in the interface region for standard configuration should produce a deterioration of spatial parameters with respect to the grease configuration. The best values (lowest mean and standard deviation) were reported for the Meltmount configuration and NN method, obtaining a $|\text{bias}_x|$ of 0.2 ± 0.2 mm and a FWHM_x of 1.0 ± 0.2 mm at the interface region; thus, achieving a uniform spatial resolution. In other experimental work, a |bias| of 0.4 mm and a FWHM of 2.1 mm was obtained at the transition region between four LYSO crystals glued together with Meltmount and applying both ML and least-squares minimization positioning estimation methods.[32] In other study, a |bias| of 0.5 mm and a FWHM of 1.5 mm near the optical coupling ($n_{grease} = 1.7$) was reported using the ML positioning estimation and simulated data.[31] We assume that the improvement in spatial performance obtained in our work is due to the use of machine-learning artificial NN techniques for positioning estimation.

Concerning DOI performance at the interface region, narrower DOI histograms were obtained for grease and standard configurations (Figure 11), because in these

TABLE 2 Spatial and energy performance obtained at the interface region for each configuration

	Spatial				Energy
	$\lvert bias_X \rvert$ (mm)		$FWHM_X$ (mm)		
	SC	NN	SC	NN	Resolution (%)
Meltmount	0.3 ± 0.2	0.2 ± 0.2	1.7 ± 0.3	1.0 ± 0.2	18 ± 2%
Grease	0.6 ± 0.5	0.4 ± 0.4	2.4 ± 0.3	1.2 ± 0.2	20 ± 2%
Standard	0.6 ± 0.5	0.5 ± 0.4	2.6 ± 0.4	1.2 ± 0.3	23 ± 3%

cases, the LD is no longer preserved, either by internal reflections or its truncation. However, for the Meltmount configuration, the LD is almost preserved and, therefore, the measured DOI histogram follows the shape of the theorical DOI distribution.[2] Out of the scope of this work, lateral incident experiments would be required to accurately estimate the DOI resolution for each configuration.

Regarding energy performance, Figure 12 shows that in the Meltmount and grease configurations, some optical photons will be collected by the neighbor crystal, thus reaching an energy fraction closer to the unit. However, it is uncleared the origin of the observed asymmetric behavior around the interface region for the standard configuration (Figure 12b). Probably, some inhomogeneities on the crystal and/or on the SiPM array could explain this behavior. For instance, an electronic read-out or paint coupling problem for column 9 of the SiPM array (Figure 5) could explain the asymmetric energy performance behavior we have observed for the standard configuration. Moreover, the best average energy resolution value was obtained for Meltmount configuration, improving the energy performance at the interface region.

Table 2 summarizes the obtained spatial and energy parameter values for each configuration at the interface region. Overall, the Meltmount configuration and NN technique allow to reduce border effects in terms of an improved spatial and energy performance.

5 | CONCLUSIONS

We have experimentally studied the effect of gluing two monolithic LYSO crystals of 33 × 25.4 × 10 mm^3 using a high refractive index compound. We have demonstrated the edge-effect reduction when optically coupling side-by-side scintillation crystals using a compound with a refractive index $n_{Meltmount} = 1.7$. We have also shown that compression effects are further reduced when using NN techniques for the gamma-ray impact position estimation in contrast to analytical methods.

It can be concluded that this approach helps increasing the light transfer between adjacent crystals in monolithic detectors, improving the uniformity of spatial and energy performance. In this way, the design and implementation of molecular imaging scanners with minimum gaps among detector blocks would be possible, enhancing the system sensitivity and performance.

In order to extrapolate this approach to PET systems, monolithic crystals that are curved could be glued together, ensuring no gaps between blocks in the transaxial axis. Our team is currently building a dedicated breast PET system based on a ring made out of 14 monolithic curved surface LYSO crystals glued together using Meltmount and read out using flexible Printed Circuit Boards (PCBs) coupled to SiPM photosensors.

ACKNOWLEDGMENTS

This work was supported in part by the Spanish Ministerio de Ciencia e Innovacion under grant no. PID2019-107790RB-C21 and by the National Institute of Health under grant no. 1R01EB029450-01. Action cofinanced by the European Union through the Programa Operativo del Fondo Europeo de Desarrollo Regional (FEDER) of the Comunitat Valenciana (IDIFEDER/2021/004).

M. Freire was supported by the BEFPI Program for Researchers in Predoctoral Phase of the Generalitat Valenciana. A. Gonzalez-Montoro is supported by VALi+d Program for Researchers in Postdoctoral Phase of the Ministry of Labor and Social Economy (Generalitat Valenciana) and the EU Social Fund.

CONFLICTS OF INTEREST

The authors have no relevant conflicts of interest to disclose.

DATA AVAILABILITY STATEMENT

The data supporting the results of this study are available upon reasonable request to the corresponding author.

REFERENCES

1. Del Guerra A, Belcari N, Bisogni MG. Positron emission tomography: its 65 years. *La Rivista del Nuovo Cimento*. 2016;39:155-223.
2. Gonzalez-Montoro A, Benlloch JM, Gonzalez AJ, et al. Performance study of a large monolithic LYSO detector with accurate photon DOI using retroreflector layers. *Trans Radiat Plasma Med Sci*. 2017;1(3):229-237.

3. González-Montoro A, Sánchez F, Bruyndonckx P, Cañizares G, Benlloch JM, González AJ. Novel method to measure the intrinsic spatial resolution in PET detectors based on monolithic crystals. *Nucl Instrum Meth A*. 2019;920:58-67.
4. Schaart DR, Van Dam HT, Seifert S, et al. A novel, SiPM-array based, monolithic scintillator detector for PET. *Phys Med Biol.* 2009;54:3501-3512.
5. Maas MC, Van Der Laan DJ, Schaart DR, et al. Experimental characterization of monolithic-crystal small animal PET readout by APD arrays. *IEEE Trans Nucl Sci.* 2006;53(3):1071-1077.
6. Gonzalez AJ, Aguilar A, Conde P, et al. A PET detector based on SiPM and monolithic LYSO crystals: performance evaluation. *IEEE Trans Nucl Sci.* 2016;63:2471-2477.
7. Cabello J, Barrillon P, Barrio J, et al. High resolution detectors based on continuous crystals and SiPMs for small animal PET. *Nucl Instrum Meth A*. 2013;718:148-150.
8. Sánchez F, Orero A, Soriano A, et al. ALBIRA: a small animal PET/SPECT/CT imaging system. *Med Phys.* 2013;40(5): 051906.
9. Moliner L, González AJ, Soriano A, et al. Design and evaluation of the MAMMI dedicated breast PET. *Med Phys.* 2012;39:5393-5404.
10. Krishnamoorthy S, Blankemeyer E, Mollet P, Surti S, Van Holen R, Karp JS. Performance evaluation of the MOLECUBES β-CUBE—a high spatial resolution and high sensitivity small animal PET scanner utilizing monolithic LYSO scintillation detectors. *Phys Med Biol.* 2018;63(15):155013.
11. Gonzalez-Montoro A, Gonzalez AJ, Pourashraf S, et al. Evolution of PET detectors and event positioning algorithms using monolithic scintillation crystals. *IEEE Trans Radiat Plasma Med Sci.* 2021;5:282-305.
12. Maas MC, Schaart DR, Van Der Laan DJ(J), et al. Monolithic scintillator PET detectors with intrinsic depth-of-interaction correction. *Phys Med Biol.* 2009;54(7):1893-1908.
13. Conde P, González AJ, Hernández L, et al. Statistical moments of scintillation light distribution analysis with dSiPMs and monolithic crystals. In 2013 IEEE Nuclear Science Symposium and Medical Imaging Conference (2013 NSS/MIC). 2013, October. (pp. 1-4). IEEE.
14. Seifert S, Van Dam HT, Huizenga J, et al. Monolithic LaBr3:Ce crystals on silicon photomultiplier arrays for time-of-flight positron emission tomography. *Phys Med Biol.* 2012;57:2219-2233.
15. Conde P, Iborra A, González AJ, et al. Minimization of border effects in monolithic scintillators using neural networks, based on MR-compatible SiPM arrays. *In EJNMMI Phys*. 2014; (Vol. 1, No. 1, pp. 1-2). SpringerOpen.
16. Vaska P, Petrillo MJ, Muehllehner G. Virtual PMTs: improving centroid positioning performance near the edges of a gamma camera detector. *IEEE Trans Nucl Sci.* 2001;48:645-649.
17. Pani R, Vittorini F, Cinti MN, et al. Revisited position arithmetics for LaBr 3:Ce continuous crystals. *Nucl Phys B Proc Suppl.* 2009;197:383-386.
18. Pani R, Nourbakhsh, S, Pani P, et al. Continuous DOI determination by Gaussian modelling of linear and non-linear scintillation light distributions. In 2011 IEEE Nuclear Science Symposium Conference Record (2011, October). (pp. 3386-3389). IEEE.
19. Di Francesco A, Bugalho R, Oliveira L, et al. TOFPET 2: a high-performance circuit for PET time-of-flight. *Nucl Instrum Meth A*. 2016;824:194-195.
20. Nadig V, Schug D, Weissler B, Schulz V. Evaluation of the PETsys TOFPET2 ASIC in multi-channel coincidence experiments. *EJNMMI Phys.* 2021;8:30.
21. Lerche ChW, Ros A, Monzó JM, et al. Maximum likelihood positioning for gamma-ray imaging detectors with depth of interaction measurement. *Nucl Instrum Meth A*. 2009;604:359-362.
22. Pierce LA, Pedemonte S, Dewitt D, et al. Characterization of highly multiplexed monolithic PET/gamma camera detector modules. *Phys Med Biol*. 2018;63:075017.
23. Zhi L, Wedrowski M, Bruyndoncx P, Vandersteen G. Nonlinear least-squares modeling of 3D interaction position in a monolithic scintillator block. *Phys Med Biol.* 2010;55:6515-6532.
24. Van Dam HT, Seifert S, Vinke R, et al. Improved nearest neighbor methods for gamma photon interaction position determination in monolithic scintillator PET detectors. *IEEE Trans Nucl Sci.* 2011;58:2139-2147.
25. Aldawood S, Thirolf PG, Miani A, et al. Development of a Compton camera for prompt-gamma medical imaging. *Radiat Phys Chem.* 2017;140:190-197.
26. Freire M, Gonzalez-Montoro A, Sanchez F, Benlloch JM, Gonzalez AJ. Calibration of gamma ray impacts in monolithic-based detectors using Voronoi diagrams. *IEEE Trans Radiat Plasma Med Sci.* 2020;4:350-360.
27. Conde P, Iborra A, Gonzalez AJ, et al. Determination of the interaction position of gamma photons in monolithic scintillators using neural network fitting. *IEEE Trans Nucl Sci.* 2016;63:30-36.
28. Gostojić A, Tatischeff V, Kiener J, et al. Characterization of LaBr3:Ce and CeBr3 calorimeter modules for 3D imaging in gamma-ray astronomy. *Nucl Instrum Meth A*. 2016;832: 24-42.
29. Ulyanov A, Morris O, Roberts OJ, et al. Localisation of gamma-ray interaction points in thick monolithic CeBr3 and LaBr3:Ce scintillators. *Nucl Instrum Meth A*. 2017;844:81-89.
30. Babiano V, Caballero L, Calvo D, Ladarescu I, Olleros P, Domingo-Pardo C. γ-Ray position reconstruction in large monolithic LaCl3(Ce) crystals with SiPM readout. *Nucl Inst Meth A*. 2019;931:1-22.
31. Vinke R, Levin CS. A method to achieve spatial linearity and uniform resolution at the edges of monolithic scintillation crystal detectors. *Phys Med Biol.* 2014;59:2975-2995.
32. Morrocchi M, Hunter WCJ, Del Guerra A, et al. Evaluation of event position reconstruction in monolithic crystals that are optically coupled. *Phys Med Biol.* 2016;61:8298-8320.
33. Cargille, Optical Mounting Media – Meltmount, DATASHEET from https://www.cargille.com/mounting-media/
34. Silicone Solutions. SS-988 Non-Curing Optical Coupling Gel - V-788 Offset DATASHEET from https://siliconesolutions.com/media/pdf/SS-988TDS.pdf. Accessed 2020.
35. Landi G. Properties of the center of gravity as an algorithm for position measurements. *Nucl Instrum Meth A*. 2002;485:698-719.
36. Ling T, Lewellen TK, Miyaoka RS. Depth of interaction decoding of a continuous crystal detector module. *Phys Med Biol.* 2007;52:2213. https://www.cargille.com/mounting-media/
37. Pani R, et al. Continuous DOI determination by Gaussian modelling of linear and non-linear scintillation light distributions. In Proceedings of IEEE NSS-MIC. 2011.
38. Lerche CW, Ros A, Herrero V, et al. Dependency of energy-, position- and depth of interaction resolution on scintillation crystal coating and geometry. *IEEE Trans Nucl Sci*. 2008;55(3):1344-1351.

How to cite this article: Freire M, Echegoyen S, Gonzalez-Montoro A, Sanchez F, Gonzalez AJ. Performance evaluation of side-by-side optically coupled monolithic LYSO crystals. *Med Phys*. 2022;49:5616-5226.
https://doi.org/10.1002/mp.15792